

1 Monitoring monthly tropical humid forest disturbances with Planet 2 NICFI images in Cameroon

3 Yihang Zhang ^{1,2*#}, Xia Wang ^{4#}, Xiaodong Li ¹, Yun Du ¹, Peter M. Atkinson ^{2,3}

- 4 1. Key Laboratory of Monitoring and Estimate for Environment and Disaster of Hubei province,
5 Innovation Academy for Precision Measurement Science and Technology, Chinese Academy of
6 Sciences, Wuhan 430077, China;
- 7 2. Lancaster Environment Center, Faculty of Science and Technology, Lancaster University,
8 Lancaster LA1 4YQ, UK;
- 9 3. Geography and Environmental Science, University of Southampton, Highfield, Southampton
10 SO17 1BJ, UK;
- 11 4. CAS Key Laboratory of Aquatic Botany and Watershed Ecology, Wuhan Botanical Garden,
12 Chinese Academy of Sciences, Wuhan 430074, China;

13 (*Corresponding author: zhangyihang@apm.ac.cn; #These authors contributed equally to this article)

14 **Abstract:** Selective logging and smallholder clearing are the dominant drivers of tropical forest
15 disturbances in Cameroon (CAM). However, they are difficult to monitor accurately by satellite remote
16 sensing because openings in the canopy can be very small, the vegetation is generally fast-growing, and
17 cloud cover is common. Norway's International Climate and Forest Initiative (NICFI) provides access to
18 monthly and biannual collections of 5 m Planet images in the tropics, creating a great opportunity for
19 mapping tropical forest disturbances. In this paper, we develop a method to monitor monthly small-scale
20 tropical humid forest disturbances using 2021 Planet NICFI images. First, a cloud mask for each of the
21 monthly Planet NICFI images was predicted by integrating a cloud cover possibility map with a haze
22 optimal transformation (HOT) index image. Second, possible monthly forest disturbances were mapped
23 from a self-referenced Hue_forest (rHue_forest) index image. Finally, an adjusted monthly forest
24 disturbance map was produced by eliminating many false positives with a spatio-temporal filter. Results
25 in CAM demonstrated that the method applied to monthly Planet NICFI images was effective in
26 identifying numerous small-scale tropical forest disturbances that were short-lived, lasting only a few
27 months. After filtering out new possible forest disturbances in 2021 which did not meet a temporal
28 permanence criterion based on the monthly images, the adjusted user's and producer's accuracies for
29 CAM were $84.7 \pm 2.9\%$ and $61.5 \pm 46.4\%$, respectively ($\pm 95\%$ confidence intervals). Our results provide
30 much greater spatial detail than forest disturbance methods based on Sentinel-1 and Landsat images. The
31 adjusted disturbed area of humid forests in CAM was estimated as $1,168 \pm 882 \text{ km}^2$ in 2021. The
32 proposed method for monthly mapping of forest disturbance using Planet NICFI images has great

33 potential to complement existing forest cover change products and monitor hitherto neglected tropical
34 forest disturbances due to small-scale clearing.

35 **Keywords:** Forest disturbance, Planet NICFI, selective logging, smallholder clearing, Cameroon.

36 **1. Introduction**

37 The world's tropical forests hold more than half of the global aboveground carbon stocks and
38 provide immense environmental and economic value, not least through their role in the global carbon
39 cycle (Baccini et al., 2017). During the past three decades, 17% of the world's tropical forests were
40 deforested and 10% degraded at the pantropical scale (Vancutsem et al., 2021), leading to massive
41 changes in carbon flux and biodiversity losses (Baccini et al., 2017; Gibson et al., 2011). Satellite-derived
42 monitoring of tropical forest disturbances is needed urgently to support tropical forest conservation and
43 promote sustainable tropical forest uses (Dong et al., 2012; Hansen et al., 2013; Qin et al., 2019;
44 Vancutsem et al., 2021; Zhu and Woodcock, 2014).

45 Satellite sensor images with various spatial resolutions ranging from 10 m to 250 m have been used
46 widely to map tropical forest disturbances (Bullock et al., 2020; Hethcoat et al., 2019; Reiche et al., 2021;
47 Tang et al., 2019; Zhang et al., 2019; Zhang et al., 2021). During the past two decades, it is noteworthy
48 that many ready-to-use remote sensing-based forest cover change products were developed, and they can
49 be applied to monitor tropical forest disturbances (Table 1). For example, Hansen et al. (2002) developed
50 the annual MODIS Vegetation Continuous Fields (VCF) product to monitor global tree canopy cover
51 dynamics since 2001, but its spatial resolution of 250 m is too coarse to provide sufficient spatial detail
52 (Francini et al., 2020). As solutions, Sexton et al. (2013) and Vancutsem et al. (2021) applied Landsat
53 images to map 30 m global VCF and forest cover changes every five years. Shimada et al. (2014) used
54 ALOS/ALOS-2 PALSAR/PALSAR-2, a dual-pole L-band Synthetic Aperture Radar (SAR), during
55 2007-2010 and 2015-2017 to estimate global forest cover maps with a spatial resolution of 25 m. Hansen
56 et al. (2013) released an annual 30 m global forest change (GFC) map since 2001. Among the ~30-m
57 scale products, the GFC product has the outstanding capability to monitor large-scale forest disturbances,
58 but the annual updating frequency remains too coarse to monitor the sub-annual tropical forest
59 disturbances (Francini et al., 2020).

60 To provide near real-time monitoring of tropical forest disturbances, Hansen et al. (2016) developed
61 a 30 m tropical forest disturbance (loss) alerting system based on all available Landsat images, which

62 was released in Global Land Analysis & Discovery (GLAD). Although Landsat has a 16-day revisit
 63 period, the extremely frequent cloud cover in the tropics limits the application of the GLAD forest loss
 64 alerting product (Francini et al., 2020; Zhang et al., 2018; Zhang et al., 2021). Watanabe et al. (2021)
 65 developed a 50 m spatial resolution near real-time forest early warning system in the tropics (JJ-FAST)
 66 by using ALOS-2 PALSAR-2 mosaics during 2019-2022. JJ-FAST can be applied in all weather
 67 conditions by taking advantage of the PALSAR-2, L-band's capacity to penetrate smoke, clouds and
 68 heavy rain. Moreover, Reiche et al. (2021) developed a 10 m forest disturbance alerting system based on
 69 Sentinel-1 C-band SAR images, with the benefit of penetrating smoke, clouds and rain and a finer spatial
 70 resolution compared to Landsat and PALSAR-2 images. However, Sentinel-1 imagery is heavily affected
 71 by noise pixels and topographic conditions, and it has the challenge of separating accurate noise pixels
 72 from some forest disturbance pixels, particularly for the mono-temporal Sentinel-1 image (Francini et
 73 al., 2020; Hethcoat et al., 2021; Zhao et al., 2022).

74 Table 1. Summary of global and pantropical forest cover change monitoring products based on various satellite
 75 images.

Name	Spatial resolution	Updating frequency	Available period	Data source	Spatial extent	Prediction model	Affiliation	Reference
RADD forest alert	10 m	6-12 days	Since 2019	Sentinel-1	Tropics	Probabilistic algorithm	Wageningen University	Reiche et al. (2021)
GLAD forest loss alert	30 m	16 days	Since 2001	Landsat	Tropics	Machine learning	University of Maryland	Hansen et al. (2016)
Global forest change (GFC)	30 m	Annual	Since 2001	Landsat	Global	Machine learning	University of Maryland	Hansen et al. (2013)
Global Forest/Non-forest Map	25 m	Annual	2007-2010, 2015-2017	ALOS/ALOS-2 PALSAR/PALSAR-2	Global	Segmentation	JAXA	Shimada et al. (2014)
Forest Cover Changes in the Humid Tropics	30 m	Every 5 years	1990-2019	Landsat	Tropics	Decision tree	European Commission	Vancutsem et al. (2021)
Landsat Vegetation Continuous Fields	30 m	Every 5 years	2000-2015	Landsat	Global	Machine learning	University of Maryland	Sexton et al. (2013)
JICA-JAXA Forest Early Warning System in the Tropics (JJ-FAST)	50 m	Annual	2019-2022	ALOS-2 PALSAR-2	Tropics	Segmentation	JAXA	Watanabe et al. (2021)
MOD44B Vegetation Continuous Fields	250 m	Annual	Since 2001	MODIS	Global	Machine learning	NASA	Hansen et al. (2002)

76 In Cameroon (CAM), one of the six Congo Basin countries, smallholder clearing and selective
 77 logging were the dominant drivers of tropical forest disturbances (Kleinschroth et al., 2019; Laporte et
 78 al., 2007; Tyukavina et al., 2018). Compared with large-scale forest disturbances, selective logging and

79 smallholder clearing are more difficult to monitor accurately with most satellite sensor images, due to
80 small-scale openings within the canopy, fast-growing vegetation and frequent clouds (Asner et al., 2005;
81 Francini et al., 2020; Hethcoat et al., 2021; Hethcoat et al., 2019; Zhang et al., 2021). Selective logging
82 roads in the rainforest have an average width of <7 m (Kleinschroth et al., 2019), which is finer than the
83 pixel size of most satellite sensors, including Landsat, Sentinel-2, PALSAR and Sentinel-1 (Table 1).
84 Given the narrowness of logging roads, a method utilizing the Normalized Difference Fraction Index
85 was developed to monitor tropical forest degradation, and it can be used to extract sub-pixel selective
86 logging from Landsat images (Souza et al., 2005), but the spatial distribution of sub-pixels is yet to be
87 provided (Zhang et al., 2018). Smallholder clearing and selective logging of tropical forests will be
88 followed commonly by fast-growing vegetation (e.g., shrubs and trees) within several months. To
89 monitor accurately the small-scale tropical forest disturbances due to selective logging and smallholder
90 clearings in CAM, satellite sensor images are required that have both fine spatial and temporal resolutions
91 (Francini et al., 2020; Kleinschroth et al., 2019).

92 Very fine spatial resolution (VFR) satellite sensor images, such as Quickbird, IKONOS, Worldview,
93 RapidEye, SPOT and GaoFen, can be used as alternative data sources to estimate small-scale tropical
94 forest disturbances (Franke et al., 2012; Souza et al., 2003; Wagner et al., 2019). However, the revisit
95 period of these VFR satellite sensors is always too coarse to monitor short-term tree canopy openings
96 caused by smallholder clearing and selective logging (Francini et al., 2020), and the data licenses of these
97 commercial satellites are expensive. The new PlanetScope CubeSat constellation is composed of more
98 than 200 *Dove* satellites and provides four-band multispectral images with a daily revisit time and spatial
99 resolution of 3 m. Planet is the first satellite system with a unique combination of large coverage, daily
100 frequency, and meter-level spatial resolution (Cheng et al., 2020; Roy et al., 2021; Wang et al., 2021).
101 It is noteworthy that Francini et al. (2020) applied firstly the daily 3 m PlanetScope images to map near
102 real-time forest cover changes from May 2018 to June 2019 in Tuscany, Italy, and indicated that
103 PlanetScope images were an attractive choice for fine spatio-temporal resolution tropical forest
104 disturbance mapping. However, the 3 m daily PlanetScope images are not freely available presently at a
105 large scale and the dense long-term daily fine spatial resolution images require heavy computational
106 processing. Moreover, the *Dove* satellites have an off-nadir view angle tolerance of 0-5 degrees, in which
107 a larger off-nadir view angle would affect the ability to consistently detect a particular small-scale
108 clearing or a narrow logging road over time. This may limit their potential widespread usage, especially

109 for monitoring forest disturbances on a large scale, such as the entire country of CAM.

110 With the primary objective of reducing and reversing tropical forest disturbances, Norway's
111 International Climate and Forest Initiative (NICFI) provides access to monthly and biannual collections
112 of Planet images with a spatial resolution of 4.77 m (~5 m) for the pantropical region. Covering the three
113 regions of tropical Africa, tropical Americas and tropical Asia, Planet NICFI provides biannual satellite
114 composite mosaics to users from December 2015 to August 2020 and monthly satellite composite
115 mosaics after September 2020. Planet NICFI image collections, especially the monthly mosaics, open a
116 great opportunity for monitoring tropical forest disturbances with meter-level spatial resolution and at
117 monthly temporal resolution, available in near real-time.

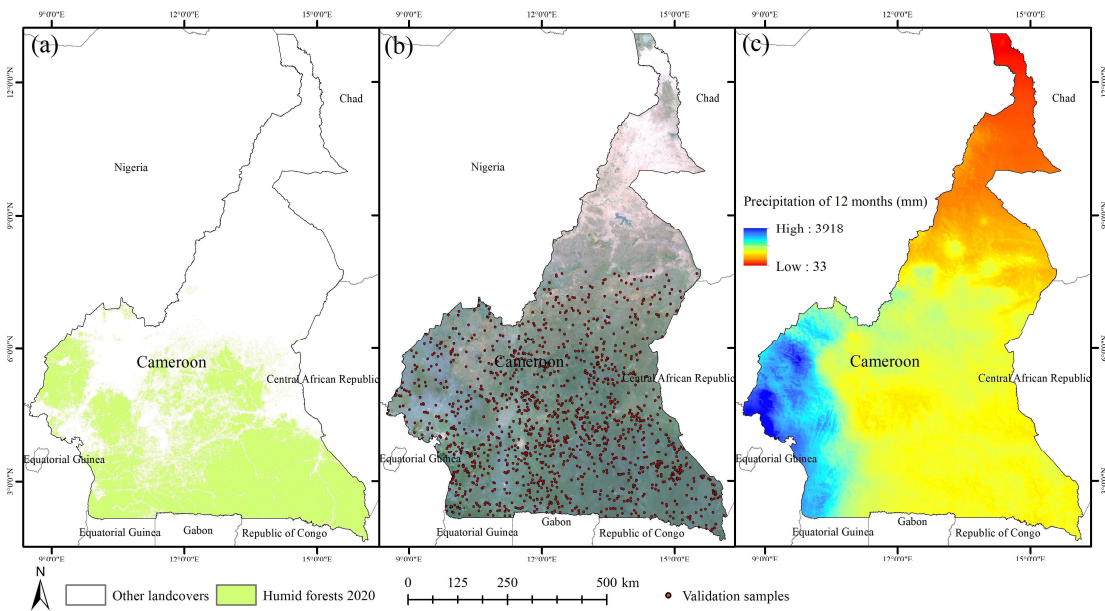
118 Given the great potential of monthly Planet NICFI images for tropical forest disturbance mapping,
119 we aim to develop a method to monitor monthly small-scale tropical humid forest disturbances based on
120 the Planet NICFI images and primary humid forest cover map. The entire CAM, which is a typical area
121 of selective logging and smallholder clearing in the Congo's tropical forests (Tyukavina et al., 2018),
122 was chosen as the study site, and it is expected to use the proposed method to monitor hitherto neglected
123 humid small-scale forest disturbances dominated by selective logging and smallholder clearing in CAM
124 during 2021.

125 **2. Study site and dataset**

126 As shown in Fig. 1, the entire CAM, with an area of 475,442 km², was selected as the study site.
127 Similar to the other five Congo Basin countries, CAM has a humid and hot climate, particularly in the
128 south. The rainfall season in CAM is from May to October, with maximum rainfall in July and August,
129 and the temperature is relatively stable between 22°C and 25°C. Agricultural smallholder clearing and
130 industrial selective logging are the top-two dominant drivers of Congo's tropical forest disturbances
131 (Kleinschroth et al., 2019; Tyukavina et al., 2018). Specifically, based on the Landsat images during
132 2001-2014 and stratified sampling method, Tyukavina et al. (2018) found that ~80% of the forest
133 disturbances in CAM was caused by small-scale forest disturbance, in which smallholder clearing was
134 the largest driver of forest disturbances and contributed about $58.0 \pm 8.0\%$ of the total loss area and the
135 percentage of selective logging was $21.8 \pm 7.9\%$. By analyzing two widely used humid tropical forest
136 disturbances based on Landsat images (Hansen et al., 2016) and Sentinel-1 images (Reiche et al., 2021),
137 we found that there were more forest disturbances during 2021 in CAM than in Gabon and Republic of

138 Congo. Thus, CAM was selected as the study site to monitor the representative selective logging and
139 smallholder clearing of tropical forests.

140 The proposed method aims to produce a monthly forest disturbance map for CAM in 2021, and it
141 is based on two types of datasets. Firstly, a primary humid forest cover map in 2020 (Fig. 1(a)) was
142 generated using the humid tropical forest cover map in 2001 (Turubanova et al., 2018), annual forest loss
143 map during 2001-2020 in GFC product (Hansen et al., 2013), RADD Sentinel-1 forest disturbances map
144 during 2019-2020 (Reiche et al., 2021), Landsat tree canopy height in 2020 (Potapov et al., 2021) and
145 Sentinel-2 land cover map in 2020 (Zanaga et al., 2021). It is noteworthy that the minimum disturbance
146 patch size detection thresholds used for the GFC product and RADD Sentinel-1 forest disturbances map
147 are 0.5 ha (~6 pixels of 30 m × 30 m) and 0.2 ha (20 pixels of 10 m × 10 m), respectively (Hansen et al.,
148 2013; Reiche et al., 2021). Detailed processing of the primary humid forest cover map will be described
149 in section 3.2.1.



150
151 Fig. 1. Humid tropical forest cover map, Planet NICFI images, reference validation points and annual precipitation
152 for the study site of CAM. (a) Primary humid tropical forest cover map in 2020; (b) Planet NICFI RGB true colour
153 image in December 2021 and 1400 reference random validation samples (see Table 2); (c) 1000 m spatial resolution
154 annual precipitation based on monthly precipitation during 2007-2019.

155 Secondly, monthly four-band Planet NICFI mosaic images around 2021 were used as input data, as
156 illustrated in Fig. 1(b). These monthly Planet basemaps were preprocessed by NICFI in Google Earth
157 Engine (GEE) platform, with the spatial resolution unified to 5 m, and they are freely available via
158 <https://www.planet.com/nicfi/> after registration. The Planet NICFI mosaic image includes four bands of

159 blue, green, red and near-infrared, in which the bit depth of each band is 16 bits, and the pixel values of
160 each band were converted to surface reflectance. The Planet NICFI mosaics were composed of images
161 from hundreds of different *Dove/Superdove* satellite sensors. To amalgamate different sensors into the
162 mosaic, normalization and harmonization operations are required to intercalibrate the differences
163 between the sensors. Moreover, a standard scene selection algorithm and co-registration with many
164 ground control points (GCPs) were used for the Planet NICFI mosaics to provide acceptable geolocation
165 error. More detailed information about Planet NICFI mosaic images can be found in
166 https://assets.planet.com/docs/NICFI_Basemap_Spec_Addendum.pdf.

167 Following Francini et al. (2020), we used the stratified random sampling method to validate the
168 monthly forest disturbance maps produced by the proposed method in CAM (Cochran, 1977; Stehman,
169 2014). The monthly forest disturbance map is produced with a spectral index, and the detailed processing
170 will be described in the later section 3.2. As shown in Table 2, 14 strata, including a total of 1400
171 validation sample points extracted from the primary humid forest cover map and monthly forest
172 disturbance map, were used in the stratified random sampling, in which two of the strata belong to the
173 category of “non-forest disturbances” and the others are in the category of “monthly forest disturbances”.
174 Due to the monthly adjusted forest disturbance map in 2021 were produced based on the primary humid
175 forest cover map in 2020, the strata of “stable humid forest” and “other land covers” were used together
176 with the stratum of “forest disturbance at t_i ” (t_i means Jan. to Dec. in 2021. The sample size of 400 was
177 allocated to the strata of “stable humid forest” and “other land covers”, respectively, while the sample
178 size of 50 was allocated to the stratum of “forest disturbance at t_i ” for each of the months in 2021. The
179 stratum label of each sample point is determined by the stratum associated with the stratification layer in
180 which the sample point is located. Specifically, the time-series monthly Planet NICFI images were used
181 for the determination process based on visual interpretation. The sampling unit (spatial size) refers to the
182 $5\text{ m} \times 5\text{ m}$ Planet image pixel. To decrease the uncertainty of visual interpretation, three experienced
183 interpreters interpreted visually the reference class of each sample unit with the help of time-series
184 monthly Planet NICFI images and very fine spatial resolution (e.g., 0.5 m) Google Earth images
185 (McRoberts et al., 2018), and the disagreement frequency among them was 32.43%. It is noted that the
186 latest (circa 2022) Google Earth images contain finer spatial resolution tree canopy cover information
187 than the 5 m Planet NICFI images, and they can be used to determine whether a sample belongs to stable
188 humid forest or other land covers. Finally, the majority reference class predicted visually among the three

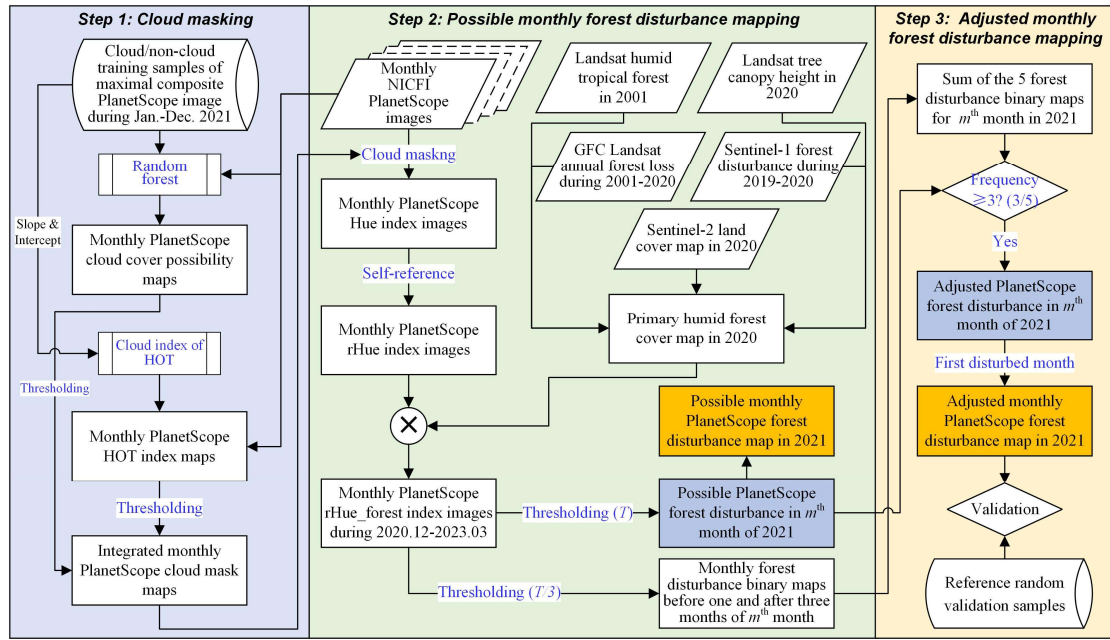
189 interpreters was used as the reference.

190 Table. 2. Summary of the strata used to validate the possible and adjusted monthly forest disturbance maps.

Category	Stratum	Sample size	Stratum size (pixels)	Source
Non-forest disturbances	Other land covers	400	0.79×10^{10}	Primary humid forest cover map & adjusted monthly forest disturbance map
	Stable humid forest	400	0.72×10^{10}	
Monthly forest disturbances	Jan.	50	3.53×10^6	adjusted monthly forest disturbance map
	Feb.	50	5.99×10^6	
	Mar.	50	8.83×10^6	
	Apr.	50	6.81×10^6	
	May	50	2.29×10^6	
	Jun.	50	0.72×10^6	
	Jul.	50	0.17×10^6	
	Aug.	50	0.38×10^6	
	Sep.	50	1.43×10^6	
	Oct.	50	1.07×10^6	
	Nov.	50	1.26×10^6	
	Dec.	50	1.42×10^6	

191 3. Methodology

192 The proposed method comprises three main steps as shown in Fig. 2: 1) predict a cloud mask for
193 each of the monthly Planet images by integrating the cloud cover possibility map and haze optimal
194 transformation (HOT) index map; 2) produce a possible monthly forest disturbance map from the self-
195 referenced Hue_forest (rHue_forest) index based on the cloud-masked Planet images and primary humid
196 forest cover map; 3) produce an adjusted monthly forest disturbance map by eliminating false positives
197 with a spatio-temporal filter, which requires at least three out of five consecutive observations (one before
198 the present observation and three after the present) to confirm each of the possible disturbances at present.
199 Step 1 is used to mask the cloud in the monthly Planet images, which are used as one of the input data
200 of step 2 to produce the possible monthly forest disturbance map, and step 3 is used to produce the
201 adjusted monthly forest disturbance map by eliminating many false positives.



202

203 Fig. 2. The proposed methodology.

204 **3.1 Cloud masking of monthly Planet NICFI images**

205 Due to the lack of SWIR bands, cloud estimation for the four-band (e.g., Blue, green, red and Nir)
 206 satellite sensor images is always a challenging task for Planet imagery. The usable data mask
 207 (UDM/UDM2) layer developed by the Planet team was used to remove cloud and cloud shadow pixels
 208 during the generation of the monthly Planet NICFI composite images, but many clouds still remain
 209 (Frazier and Hemingway, 2021; Pascual et al., 2022). Our research used two methods to predict any
 210 clouds in the monthly Planet NICFI images. For each of the monthly Planet images, the random forests
 211 (RF) machine learning method developed by Breiman (2001) was applied first to produce a cloud cover
 212 possibility map (Pal, 2005). In general, we could collect training samples from each of the monthly Planet
 213 NICFI images, but this would be time-consuming for the study site of CAM. Considering that cloud
 214 cover is expected to produce higher reflectance than the other land covers, the maximal composite Planet
 215 images from January to December 2021 can, thus, identify most of the clouds in the monthly images.
 216 We, therefore, collected cloud and non-cloud sample pixels by visual interpretation, which were used in
 217 the RF model to establish the cloud cover possibility map for monthly Planet NICIF images, and
 218 threshold values ranging from 20% to 40% were used to predict the cloud masks of different seasons.

219 Besides the above cloud cover possibility maps, the cloud index of “haze optimal transformation
 220 (HOT)” was also used here to create the cloud mask (Zhang et al., 2002), and it is expressed as

221
$$\text{HOT} = \frac{|a \times \rho(\text{blue}) - \rho(\text{red}) + b|}{\sqrt{1 + a^2}}, \quad (1)$$

222 where $\rho(\text{blue})$ and $\rho(\text{red})$ are the spectral reflectance values of bands 2 and 3 in the Planet image,
223 and the parameters a and b refer to the slope and intercept of the clear-sky line. The clear-sky line is a
224 linear regression adjusted in some attribute space of pixels captured under a clear sky with no cloud,
225 cloud shadow and haze, in which the axes of this attribute space are the spectral reflectance values of the
226 blue and red bands. We used the maximal composite Planet image to predict the slope and intercept. With
227 the slope and intercept estimates, HOT index images were predicted for each of the monthly Planet
228 images, and threshold values ranging from 0.016 to 0.028 were used to predict the cloud masks. The
229 optimal HOT threshold value for each monthly Planet NICFI image was chosen by comparing cloud
230 masking performance using threshold values ranging from 0.004 to 0.04 with an interval of 0.04.

231 **3.2 Possible and adjusted monthly forest disturbance mapping**

232 **3.2.1 Primary humid forest cover map in 2020**

233 Primary humid forests contain the greatest terrestrial ecosystem biodiversity compared to many
234 other forests (Betts et al., 2017; Hansen et al., 2016). In general, it is difficult to map directly the spatial
235 extent of primary humid forest cover using satellite sensor images, as the spectral and spatial features of
236 primary humid forests are similar to those of many other forests. It is noteworthy that Turubanova et al.
237 (2018) developed a baseline map of primary humid tropical forests in 2001. In this research, the annual
238 forest loss map during 2001-2020 in the GFC product developed by Hansen et al. (2013), Sentinel-1
239 forest disturbance map during 2019-2020 developed by Reiche et al. (2021), Landsat tree canopy height
240 in 2020 (Potapov et al., 2021) and Sentinel-2 land cover map in 2020 (Zanaga et al., 2021) were used to
241 predict the spatio-temporal dynamic of forest cover before 2021. To produce the primary humid forest
242 binary map in 2020, all the forest pixels marked as forest disturbance pixels in the GFC and Sentinel-1
243 forest disturbance maps before 2021 and the non-forest covers in the Sentinel-2 land cover map in 2020
244 were excluded in the baseline map. According to the report presented by Turubanova et al. (2018), the
245 average height of primary humid forest in the Democratic Republic of the Congo (DRC) ranged from 15
246 m to 29 m. Therefore, as CAM and DRC are both Congo Basin countries, the minimal average height of
247 15 m was, thus, applied to the Landsat tree canopy height in 2020 to exclude many non-humid forests in
248 the baseline map.

249 3.2.2 Self-referenced Hue_forest (rHue_forest) index

250 Although most of the clouds can be removed using the above cloud cover possibility maps and HOT
 251 index images, some small-scale clouds will remain. It is noteworthy that Francini et al. (2020) have
 252 illustrated firstly the superiority of the Hue index in near real-time forest disturbance detection with
 253 PlanetScope images. The Hue index has the advantage of being robust to clouds and cloud shadows, with
 254 small values for clouds and cloud shadows pixels, but large values for forest cleared pixels (Francini et
 255 al., 2020). The Hue index (<https://www.indexdatabase.de/db/i-single.php?id=34>) is expressed as,

$$256 \text{ Hue} = \arctg\left(\frac{2 \times \rho(\text{red}) - \rho(\text{green}) - \rho(\text{blue})}{30.5} \times (\rho(\text{green}) - \rho(\text{blue}))\right) \quad (2)$$

257 where $\rho(\text{red})$, $\rho(\text{green})$ and $\rho(\text{blue})$ are the spectral reflectance values of bands 3, 2 and 1 of
 258 PlanetScope image, respectively. The Hue index is based on the arctangent function, and its value is in
 259 the range of $[-\pi/2, \pi/2]$. In this research, we focused on the Hue pixels within the primary humid forest
 260 cover map in 2020, expressed as,

$$261 \text{ Hue_forest} = \begin{cases} \text{Hue_forest} & \text{if } \text{Map_forest} = 1 \\ 0 & \text{if } \text{Map_forest} = 0 \end{cases} \quad (3)$$

262 where Map_forest is the primary humid forest binary map in 2020, and Hue_forest is the Hue index
 263 image for the primary humid forest pixels.

264 Small values of Hue_forest may be caused by illumination geometries, atmospheric conditions and
 265 seasonal phenological changes, which may potentially be confused with the signal of interest relating to
 266 small-scale openings. A focal operation for noise removal was, thus, applied to the Hue_forest index to
 267 enhance the spectral signal of small-scale forest disturbances (Langner et al., 2018; Zhang et al., 2021),
 268 expressed as,

$$269 \text{ rHue_forest}^* = \text{Hue_forest} - \text{Hue_forest}(\text{median}, r), \quad (4)$$

$$270 \text{ rHue_forest}^* = \begin{cases} 1 & \text{if } \text{rHue_forest}^* > 1 \\ 0 & \text{if } \text{rHue_forest}^* < 0 \end{cases} \quad (5)$$

$$271 \text{ rHue_forest} = \begin{cases} \text{rHue_forest}^* & \text{if } -0.1 \leq \text{Hue_forest} \leq 0.3 \\ 0.3 & \text{if } \text{Hue_forest} \geq 0.3 \\ 0 & \text{if } \text{Hue_forest} < -0.1 \end{cases}, \quad (6)$$

272 in which $\text{Hue_forest}(\text{median}, r)$ is the median filtered image of the original Hue_forest index map,
 273 produced using a circular moving kernel median filter with a radius of r , which is always set in the range
 274 200-400 m. In this research, the radius r is 300 m. rHue_forest^* in Eq. (4) is in the range -1 to 1, and any

275 negative values in it are reassigned to 0 and any values larger than 1 are set as 1 by using Eq. (5). In
 276 general, the rHue_forest* index works well for indicating forest disturbances when the maximal width of
 277 the opening in tropical forests is smaller than twice the radius of the kernel *median* filter (Langner et al.,
 278 2018). However, some large-scale tropical forest disturbance areas may remain in real the situation. Eq.
 279 (6) was, thus, used here to constrain the rHue_forest index to a large value of 0.3 if the Hue index was
 280 larger than an empirical value of 0.3. Meanwhile, in Eq. (6), rHue_forest was assigned a small value of
 281 0 if the Hue index was smaller than an empirical value of -0.1, as a very small Hue value (e.g., <-0.1)
 282 often indicates a closed forest.

283 3.2.3 Possible monthly forest disturbance mapping

284 Forest disturbance in this research is denoted as openings in the tree canopy, predicted by an increase
 285 of rHue value for the pixel of primary humid forest cover, in which the original rHue value of the forested
 286 pixel approximates 0. By iterating over the above monthly rHue_forest images from January to December,
 287 if a pixel value in the rHue_forest index image was larger than T (a threshold parameter), it was regarded
 288 as possible forest disturbance; and the first month (m) with the rHue_forest index value larger than T was
 289 identified as the forest disturbance time. Meanwhile, the rHue_forest value of pixel i at the most recent
 290 month before the observation year (e.g., 2021 in this study) should be less than T , to guarantee that the
 291 pixel has not been regarded as forest disturbance before the observation period. The monthly forest
 292 disturbance mapping process for pixel i is expressed as Eq. (6),

$$293 \quad \text{Fdt}(i, \text{first}) = \begin{cases} m \in \{1, 2, \dots, 12\} & \text{if } \text{rHue_forest}(m, i) \geq T \\ 0 & \text{otherwise} \end{cases}, \quad (7)$$

294 in which $\text{Fdt}(i, \text{first})$ means the first possible forest disturbance time of pixel i and $\text{rHue_forest}(m, i)$ is
 295 the value of rHue_forest index for pixel i at the m^{th} month in 2021.

296 3.2.4 Adjusted monthly forest disturbance mapping with spatio-temporal filter

297 The above possible monthly forest disturbance map may contain some false positives caused by
 298 remaining clouds, registration errors and spectral outliers in the time-series Planet NICFI images.
 299 Moreover, for the identification of the first month of a disturbance, if it is a very small temporal change
 300 in rHue_forest (from slightly below T to slightly above T) compared to the previous, the disturbance
 301 could be a false positive. Generally, false positives are always ephemeral and exist within a short period,
 302 but the areas caused by real forest disturbances will present continuously as bare land for several months
 303 (e.g., three months). Based on this principle, as shown in Fig. 3, we developed a spatio-temporal filter to

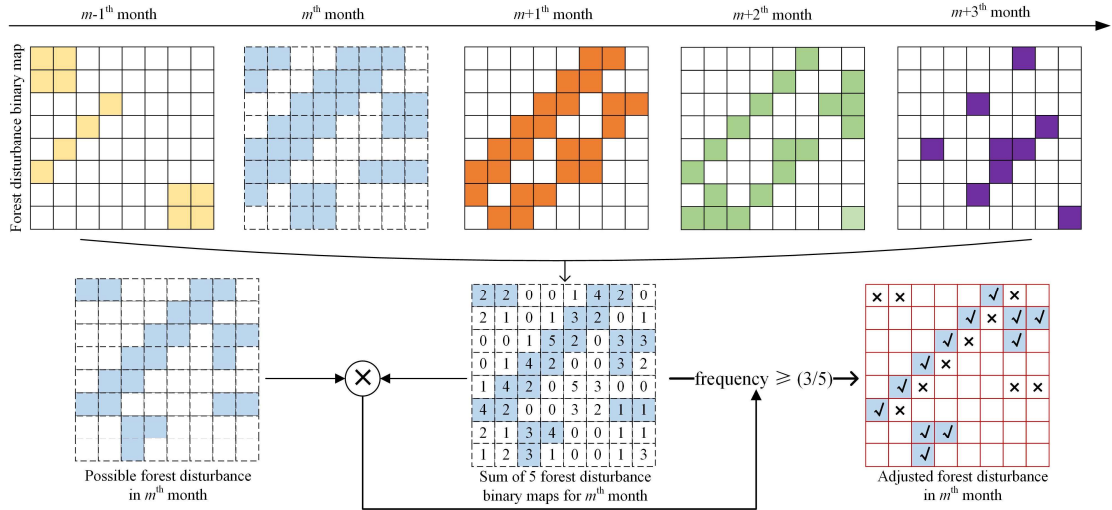
304 eliminate false positives for the adjusted monthly forest disturbance map, expressed as:

$$305 \quad \hat{Fdt}(i, first) = \begin{cases} m \in \{1, 2, \dots, 12\} & \text{if } rHue_forest(m, i) \geq T \ \& \ Fre(i) \geq 3 \\ 0 & \text{otherwise} \end{cases}, \quad (8)$$

$$306 \quad Fre(i) = \sum_{m \in P} Dis(m, i), \quad (9)$$

$$307 \quad Dis(m, i) = \begin{cases} 1, & rHue_forest(m, i) \geq T/3 \\ 0, & \text{otherwise} \end{cases}, \quad (10)$$

308 where $Fre(i)$ is the frequency of pixel i regarded as forest disturbance within the period of P months, after
 309 the month of possible first detection. The observation period P ranges from the $m-1^{th}$ to $m+3^{th}$ month,
 310 and this means there should be one month Planet image before the m^{th} month and three months Planet
 311 images after the m^{th} month. $Dis(m, i)$ is a binary function and refers to 1 if the $rHue_forest$ index value
 312 of pixel i in m^{th} month is larger than $T/3$, otherwise, it is 0. Different from using threshold value T to track
 313 the first forest disturbance time in Eq. (7), a smaller threshold value (e.g., $T/3$) used in Eq. (10) can record
 314 more unique information before and after the forest disturbance. To provide a balance between false
 315 positives and false negatives for the detected disturbances, we chose a threshold of $T = 0.09$ in this
 316 research. See section 4.3 for support of this choice. Based on the spatio-temporal filter in Eqs. (9)-(10),
 317 the adjusted forest disturbance time of pixel i can, thus, be predicted, which means that if the $rHue_forest$
 318 index value of the humid forest pixel is larger than T and the disturbing frequency is larger than 3, the
 319 first disturbing time is real, otherwise, it is a false positive. It is noteworthy that if the disturbing
 320 frequency threshold is 1, the adjusted monthly forest disturbance map would be the same as the possible
 321 monthly forest disturbance map in section 3.2.2. Finally, the forest disturbance patches, which are
 322 composed of less than 7 pixels within a neighborhood window size of 15 pixels \times 15 pixels, will be
 323 regarded as noise and deleted in the postprocessing of the possible and adjusted monthly forest
 324 disturbance maps.



325

326 Fig. 3. Illustration of using the spatio-temporal filter to estimate the adjusted monthly forest disturbance map.

327 3.3 Comparison, area and accuracy estimators

328 To provide a comprehensive validation of the performance of the proposed method based on Planet
 329 NICFI images, as listed in Table 1, two near real-time tropical forest disturbance maps based on RADD
 330 Sentinel-1 (Reiche et al., 2021) and GLAD Landsat (Hansen et al., 2016) were used as comparisons.
 331 Simultaneously, the forest loss map in the GFC product (Hansen et al., 2013), which can only provide
 332 the forest disturbing time annually, was also used as the comparison here. As the three forest disturbance
 333 maps have spatial resolutions (10 m and 30 m) coarser than the Planet images, they are used mainly for
 334 comparison of spatial distributions (i.e., visual comparison) with the monthly forest disturbance map.

335 For the area and accuracy assessments of the possible monthly forest disturbance map (section 3.2.3)
 336 and adjusted monthly forest disturbance map (section 3.2.4) in CAM, the area proportion for the
 337 reference classes, and the producer's accuracy and user's accuracy of the map classes, were used. Assume
 338 that the region of interest (i.e., the population) is partitioned into H strata with N pixels, N_h^* is the size
 339 of each stratum h ($h \in H$). Based on the stratified random sampling, n_h^* sample units are selected
 340 randomly from the N_h^* pixels of stratum h . It is noteworthy that the stratum label is extracted from a
 341 map that may be different from the map being assessed, and the method, which estimates area and
 342 accuracy using indicator functions, described by Stehman (2014) was then applied here. Firstly, the
 343 stratified estimator of the proportion of area of class k based on the indicator function can be expressed
 344 as:

345
$$\hat{p}_k^A = \frac{1}{N} \sum_{h=1}^H N_h^* \bar{y}_h^k, \quad (11)$$

346
$$\bar{y}_h^k = \sum_{u=1}^{n_h^*} y_u^k / n_h^*, \quad (12)$$

347
$$y_u^k = \begin{cases} 1, & \text{if pixel } u \text{ is reference class } k \\ 0, & \text{otherwise} \end{cases}, \quad (13)$$

348 in which \hat{p}_k^A is the proportion of area of class k , y_u^k is a binary element of class k within n_h^* samples

349 of stratum h , and \bar{y}_h^k is the sample mean of the y_u^k values that have the reference class k in stratum h .

350 An estimator of the standard error of \hat{p}_k^A is

351
$$SE(\hat{p}_k^A) = \sqrt{\frac{1}{N^2} \sum_{h=1}^H N_h^{*2} (1 - n_h^* / N_h^*) \text{Var}(y_h^k) / n_h^*}, \quad (14)$$

352 where $SE(\hat{p}_k^A)$ is the standard error and $\text{Var}(y_h^k)$ is the variance of y_u^k values of all samples that

353 have the reference class k in stratum h .

354 Secondary, the stratified estimator of producer's accuracy and user's accuracy of class k based on

355 two indicator functions can be expressed as the ratio \hat{R}_k :

356
$$\hat{R}_k = \frac{\sum_{h=1}^H N_h^* \bar{y}_h^k}{\sum_{h=1}^H N_h^* \bar{x}_h^k}. \quad (15)$$

357 where \bar{y}_h^k and \bar{x}_h^k are the sample mean of the y_u^k and x_u^k values, which are based on two indicator

358 functions. Similar to equations (12) and (13), \bar{y}_h^k is the sample mean of the y_u^k values (indicator

359 function) that have the same reference and map class k (i.e., correctly classified as class k) in stratum h .

360 If \hat{R}_k refers to the producer's accuracy, the \bar{x}_h^k is the sample mean of the x_u^k that have reference

361 class k in stratum h . By contrast, if \hat{R}_k refers to the user's accuracy, the \bar{x}_h^k is the sample mean of the

362 x_u^k that have map class k in stratum h . An estimator of the standard error of \hat{R}_k is

363
$$SE(\hat{R}_k) = \sqrt{\frac{1}{\hat{X}^2} \sum_{h=1}^H N_h^{*2} (1 - n_h^* / N_h^*) (\text{Var}(y_h^k) + \hat{R}_k^2 \text{Var}(x_h^k) - 2\hat{R}_k \text{Cov}(y_h^k, x_h^k)) / n_h^*}, \quad (16)$$

364
$$\hat{X} = \sum_{h=1}^H N_h^* \bar{x}_h^k, \quad (17)$$

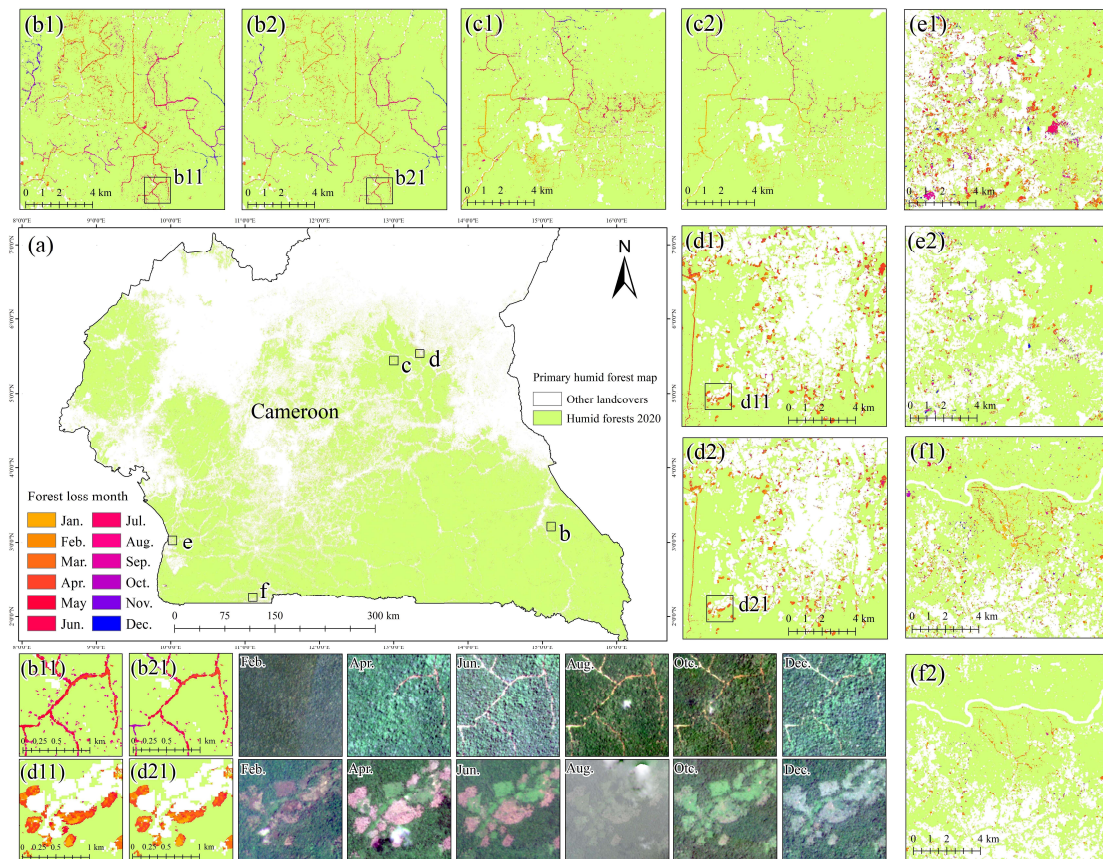
365 Where $SE(\hat{R}_k)$ is the standard error of producer's accuracy or user's accuracy, $Var(y_h^k)$ is the
366 variance of y_u^k values that have the same reference and map class k in stratum h , $Var(x_h^k)$ is the
367 variance of x_u^k values that have reference class k in stratum h if it is used for producer's accuracy and
368 that have map class k for user's accuracy, $Cv(y_h^k, x_h^k)$ is the covariance between x_u^k and y_u^k .

369 To provide approximate 95% confidence intervals for the area proportion, producer's accuracy and
370 user's accuracy, $\hat{\mu} \pm 1.96 \cdot SE(\hat{\mu})$ was used here, where $\hat{\mu}$ is the target parameter to be estimate and SE
371 is the standard error of the estimate (Francini et al., 2020; Olofsson et al., 2014).

372 **4. Results**

373 **4.1 Possible and adjusted monthly forest disturbance maps**

374 The possible and adjusted monthly forest disturbance maps in CAM are shown in Fig. 4, and five
375 zoomed areas are used to illustrate the spatial detail of the small-scale forest disturbances predicted by
376 selective logging and smallholder clearing. Forest disturbances distribute widely across the humid forests
377 in CAM, and many are along the boundaries of humid forests. Figs. 4(b1)-(b2) and Figs. 4(c1)-(c2) are
378 two typical examples of forest disturbances caused by selective logging, and the forest logging roads
379 form complex networks, in which the long main logging roads are wider than many of the short logging
380 roads along them (see Figs. 4(b11)-(b21)). Moreover, it is interesting, although not unexpected, to find
381 that there are many small-scale forest disturbances along both sides of the logging roads. Figs. 4(d1)-(d2)
382 and Figs. 4(e1)-(e2) are two typical examples of smallholder clearing and Figs. 4(f1)-(f2) are used to
383 show a mixture of selective logging and smallholder clearing. Many of the forest disturbances caused by
384 smallholder clearing hold spatial sizes larger than the small-scale forest disturbances along the selective
385 logging roads (see Figs. 4(d11)-(d21)). In all the zoomed areas, it is obvious to find that possible forest
386 disturbances are much more than the adjusted forest disturbances, such as wider selective logging roads,
387 more smallholder clearings and larger spatial extents.

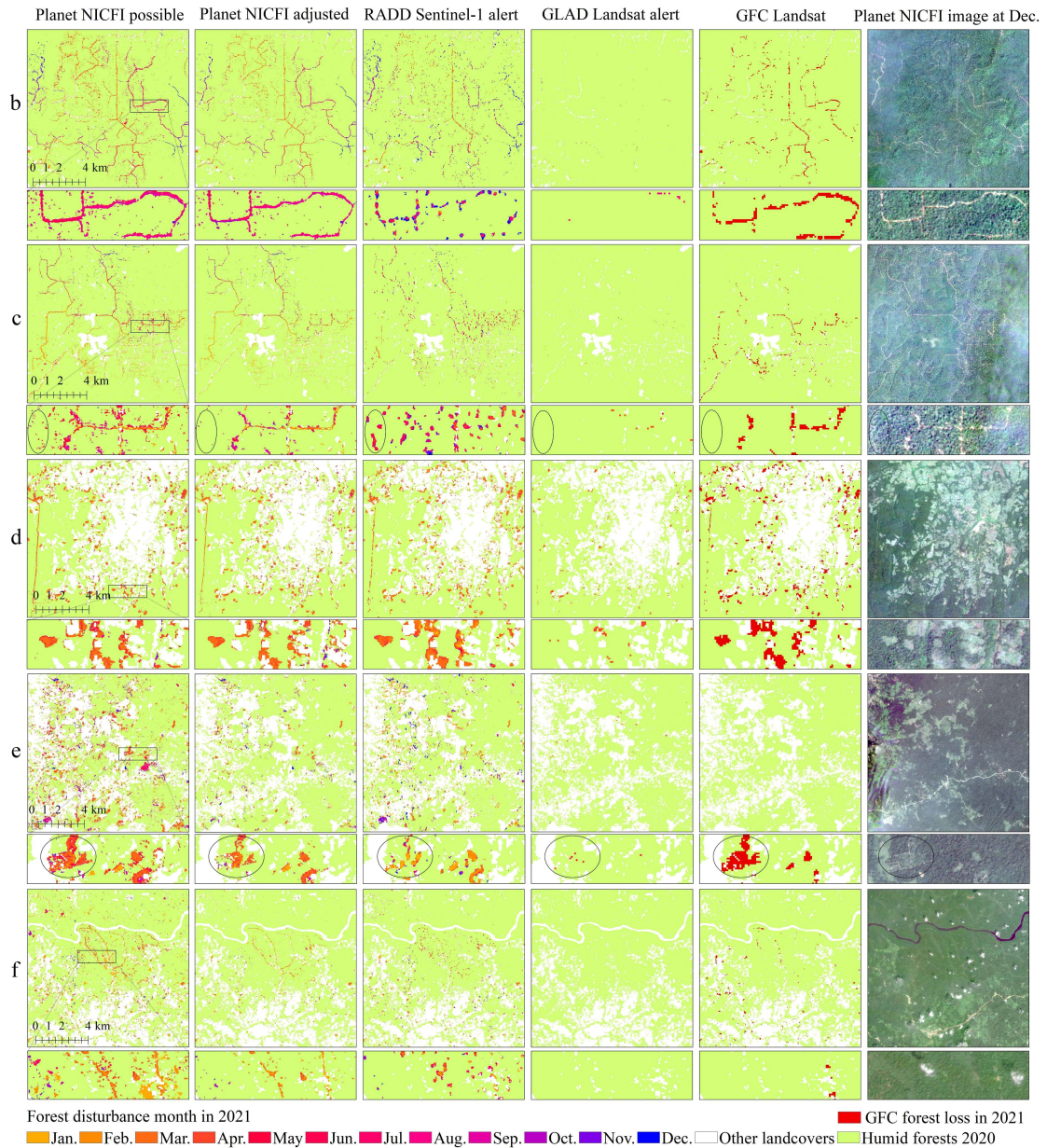


388
 389 Fig. 4. Possible and adjusted 5 m monthly forest disturbance maps of CAM in 2021 produced by the proposed
 390 method. (a) Adjusted monthly forest disturbance map of CAM in 2021; (b1)-(b2) Subset possible and adjusted forest
 391 disturbance maps caused by selective logging for location box 'b' in (a); (c1)-(c2) Selective logging; (d1)-(d2)
 392 Smallholder clearing; (e1)-(e2) Smallholder clearing; (f1)-(f2) A mixture of selective logging and smallholder
 393 clearing; (b11)-(b21) and (d11)-(d21) Zoomed areas in (b1)-(b2) and (d1)-(d2) and the time-series bimonthly Planet
 394 NICFI image.

395 The last two rows beginning at Fig. 4(b11) and Fig. 4(d11) illustrate the logging and recovery
 396 process of small-scale forest disturbances caused by selective logging and smallholder clearing,
 397 respectively. By matching the monthly forest disturbance maps with the bimonthly Planet RGB images,
 398 the expansion of logging roads and small-scale forest disturbances from February to December in the
 399 two subsites can be seen clearly. On the other hand, it can also be seen that many forest disturbances
 400 were covered again by vegetation within two-to-four months if they were abandoned after disturbance.
 401 The smaller the spatial size of forest disturbances areas, the quicker the recovery process, and this
 402 indicates that it is necessary for satellite sensor images to monitor selective logging and smallholder
 403 clearing within two-to-four months after disturbance, otherwise, the vegetation growth in the forest
 404 disturbance areas may reduce the satellite spectral signals of openings of the tree canopy (Francini et al.,
 405 2020).

406 **4.2 Comparison to other forest disturbance maps**

407 As shown in Fig. 5, the RADD Sentinel-1 alert can detect and monitor many forest disturbances
408 (particularly in the black ovals of zoomed area 'c'), but it also gives the visual impression of having been
409 smoothed by a majority filter, causing narrow logging roads to break into pieces and causing shrinkage
410 of small-holder clearing patches, particularly in the black ovals of zoomed area 'e'. This may be because
411 the accuracy decreases for detection of disturbance patches smaller than 0.2 hectares (i.e., 20 pixels)
412 Reiche et al. (2021). Compared with the results of Sentinel-1, many selective logging and smallholder
413 clearing events were missed in the results of GLAD and GFC based on Landsat images, although the
414 GFC Landsat results are preferable to the GLAD Landsat results. However, for the possible and adjusted
415 monthly forest disturbance maps based on Planet images, more forest disturbances and spatial details of
416 selective logging and smallholder clearing are identified clearly, which are more matched to the logging
417 roads and small-scale bareland in the monthly Planet RGB images in December (the last column in Fig.
418 5). Compared with the NICFI Planet possible forest disturbances, many false positives were eliminated
419 in the adjusted forest disturbances, but many real forest disturbances were also removed, as is clear from
420 the visual comparison to the Planet RGB images as references. The proposed method based on Planet
421 images can monitor many narrow logging roads and small-scale forest disturbances along the logging
422 roads, and the spatial extension process of smallholder clearing from a central point to its vicinity is also
423 predicted. This indicates the superiority of monthly Planet NICFI images in predicting the spatial and
424 temporal dynamics of small-scale forest disturbances.



425

426

427

Fig. 5. Comparison of the monthly forest disturbance maps produced from the Planet NICFI, RADD Sentinel-1 alert, GLAD Landsat alert and GFC product for the five zoomed areas in Fig. 4.

428

429

430

431

432

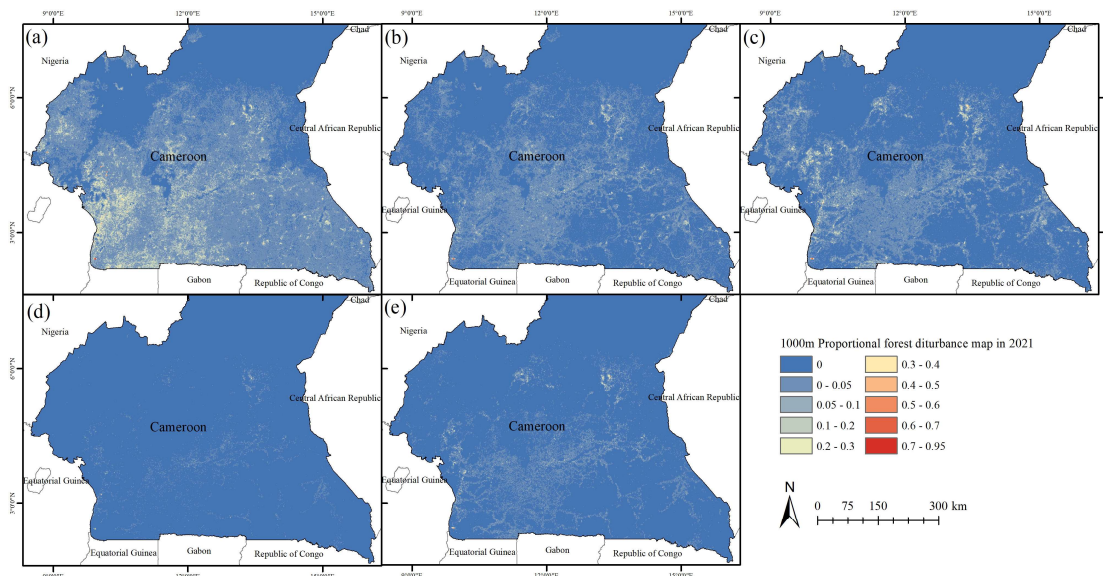
433

434

435

To provide a comprehensive comparison of the spatial distribution of forest disturbance maps extracted by the different methods, four 1 km spatial resolution proportional forest disturbance maps for CAM in 2021 are shown in Fig. 6. All the coarse spatial resolution proportional maps were predicted by spatially averaging the different fine spatial resolution forest disturbance maps. The GLAD Landsat proportional forest disturbance map has the least spatial extent of forest disturbances (see Fig. 6(d)), and there is an improvement for the GFC proportional forest disturbance map (see Fig. 6(e)). In the RADD Sentinel-1 proportional forest disturbance map, the spatial extent of forest disturbance is much more widely seen across CAM than those of GLAD and GFC based on Landsat images (see Fig. 6(c)). As

436 shown in Fig. 6(a), the proportional possible forest disturbance map produced by the proposed method
 437 has the greatest spatial extent of forest disturbance, especially in the west coast areas with frequent clouds,
 438 as it includes many false positives of forest disturbances caused by remaining clouds. In the proportional
 439 adjusted forest disturbance map of Fig. 6(b), many false positives were eliminated, and most of the forest
 440 disturbance hot spots (e.g., proportional value >0.2) match well with the those of RADD Sentinel-1 (Fig.
 441 4(c)) and GFC Landsat (Fig. 4(e)).



442
 443 Fig. 6. Comparison of proportion of 1 x 1 km cells with forest disturbances occurring in 2021, by different methods
 444 and sensors. (a) Planet NICFI proportional possible forest disturbance map; (b) Planet NICFI proportional adjusted
 445 forest disturbance map; (c) RADD Sentinel-1 proportional forest disturbance map; (d) GLAD Landsat proportional
 446 forest disturbance map; (e) GFC Landsat proportional forest disturbance map.

447 Based on the stratified estimator of the proportion of area shown in equations (10)-(13), the total
 448 adjusted forest disturbance area from January to December was estimated as $1,168 \pm 882 \text{ km}^2$ for CAM
 449 in 2021. As listed in Table 3, the possible monthly forest disturbance from January to December has the
 450 best producer's accuracy of $96.85 \pm 2.65\%$ but the least user's accuracy of $21.37 \pm 16.91\%$, which means
 451 it has many commission errors (false positives). By contrast, the adjusted monthly forest disturbance map
 452 has the best user's accuracy of $84.67 \pm 2.89\%$ by eliminating many false positives with the spatio-
 453 temporal filter, but its producer's accuracy, $61.46 \pm 46.43\%$, is not that good, which means it has many
 454 omission errors (false negatives). For the adjusted monthly forest disturbance map, the user's accuracy
 455 and producer's accuracy of other land covers and stable humid forest are $88.50 \pm 3.13\%$ and $88.71 \pm$
 456 2.72% , respectively. The accuracies of these two classes are high, but some other land covers were
 457 misclassified as humid forests, which also decreases the accuracy of monthly forest disturbance mapping

458 (e.g., leads to many false positives).

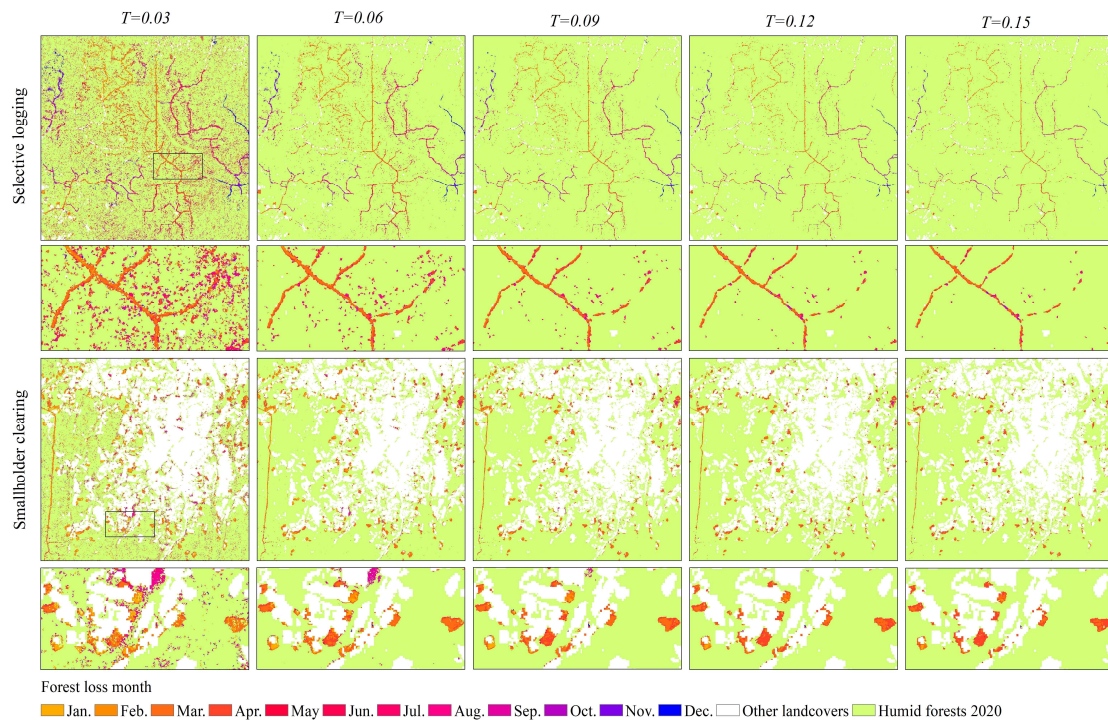
459 Table 3. Accuracy assessment and area statistics of the possible and adjusted monthly forest disturbance maps, “±”
 460 means 1.96 standard errors or, equivalently, approximate 95% confidence intervals.

Stratum	Possible monthly forest disturbance map		Adjusted monthly forest disturbance map		Area ($\times 10^4$ ha)
	Producer's accuracy	User's accuracy	Producer's accuracy	User's accuracy	
Other land covers	99.19±0.86%	87.72±3.19%	98.93±0.99%	88.50±3.13%	--
Stable humid forest	85.80±3.06%	99.19±0.88%	88.71±2.72%	98.75±1.09%	2003.91±65.06
Jan.-Dec.	96.85±2.65%	21.37±16.91%	61.46±46.43%	84.67±2.89%	11.68±8.82
Jan.	71.64±14.11%	75.12±12.62%	83.58±12.74%	84.00±10.27%	0.89±0.16
Feb.	59.91±12.60%	17.78±27.34%	75.24±10.77%	86.00±9.72%	1.71±0.28
Mar.	25.49±35.03%	25.09±33.98%	28.05±38.42%	82.00±10.76%	6.46±8.83
Apr.	90.22±8.46%	19.33±28.01%	90.66±7.20%	70.00±12.83%	1.31±0.24
May	80.25±10.38%	7.35±13.00%	84.62±7.56%	68.00±13.06%	0.46±0.08
Jun.	71.11±15.75%	2.09±4.00%	78.37±15.13%	60.00±13.72%	0.14±0.04
Jul.	74.31±27.05%	62.22±14.31%	76.97±27.51%	58.00±13.82%	0.03±0.01
Aug.	55.34±17.47%	0.67±0.93%	60.53±18.07%	70.00±12.83%	0.11±0.03
Sep.	76.21±12.14%	2.44±3.31%	84.01±9.49%	70.00±12.83%	0.30±0.06
Oct.	78.60±14.00%	65.29±14.72%	93.15±8.85%	64.00±13.44%	0.18±0.04
Nov.	86.81±11.90%	3.70±6.89%	93.01±9.04%	60.00±13.72%	0.20±0.05
Dec.	87.10±10.66%	78.57±12.54%	97.66±4.50%	74.00±12.28%	0.27±0.05

461 4.3 Effect of parameter T on monthly forest disturbance mapping

462 T in Eqs. (6)-(9) is an important parameter used to convert the rHue_forest index into a binary forest
 463 disturbance map, prior to applying the spatio-temporal permanence criterion. Given the two typical
 464 examples of selective logging and smallholder clearing, Fig. 7 illustrates the monthly forest disturbance
 465 maps using values of T ranging from 0.03 to 0.15 with an interval of 0.03. In the study site representing
 466 selective logging, small values of T lead to forest disturbance maps with wider logging roads and many
 467 small-scale forest disturbances along the roads. With an increase in T , the width of the logging roads
 468 narrows and the small-scale forest disturbances along the roads disappear eventually. Compared to
 469 selective logging, smallholder clearing is not particularly sensitive to changes in T , especially for some
 470 large-scale forest disturbed patches. When T is too small (e.g., 0.03), there exist many noise pixels,
 471 caused mainly by changes in irradiance and vegetation phenology across the monthly Planet images.
 472 When T is too large (e.g., 0.15), although many noise pixels are eliminated, some intact forest disturbance
 473 patches are separated into subset patches. Therefore, T ranging from 0.06 to 0.12 is suggested for the
 474 rHue_forest index to monitor Planet monthly forest disturbances in real applications. In this research, T

475 was set to 0.09 to eliminate many false positives and maintain sufficient real forest disturbances.



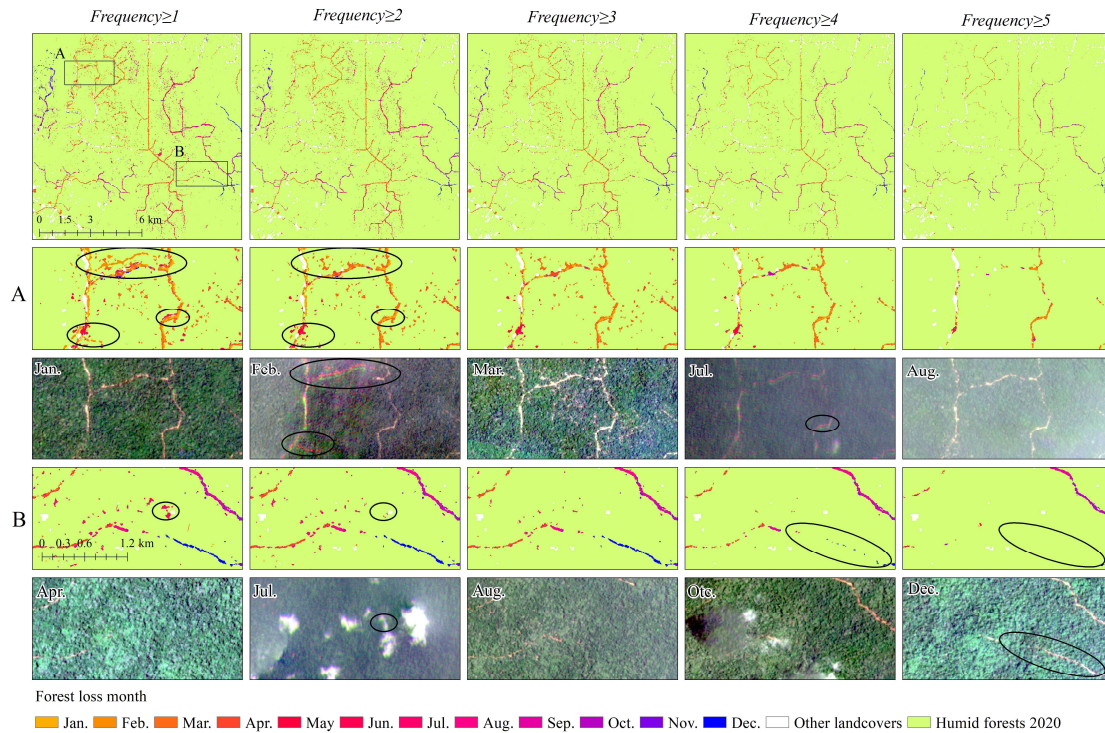
476

477 Fig. 7. An illustration of monthly forest disturbance maps for two typical examples of selective logging and
 478 smallholder clearing with T ranging from 0.03 to 0.15.

479 **4.4 Effect of spatio-temporal filter on the adjusted monthly forest disturbance mapping**

480 The disturbance frequency in the spatio-temporal filter is crucial for the adjusted monthly forest
 481 disturbance mapping in Eq. (7). Given the typical example of selective logging, Fig. 8 illustrates the
 482 monthly forest disturbance maps by using disturbance frequency thresholds ranging from 1 to 5 with an
 483 interval of 1, which is the number of months (with a cap of 5) for a new disturbance that continues to be
 484 classified as non-forest. As shown in the black oval of zoomed area A, some logging roads are presented
 485 as red and green outliers in the Planet NICFI images of February and July, and they disappeared totally
 486 in the following months of March and August. These outliers were regarded as forest disturbances in the
 487 possible forest disturbance map when the disturbing frequency threshold was no less than 1, but they
 488 were almost eliminated when the disturbance frequency threshold was no less than 2. A similar trend can
 489 also be observed for the black oval of zoomed area B, a few cloud pixels with a small size in July were
 490 not removed by the cloud masks, and they were first regarded as forest disturbances when the disturbance
 491 frequency threshold is no less than 1. However, the false positives caused by remaining clouds shown in
 492 in zoomed area B were also eliminated when the disturbance frequency threshold was no less than 2 or
 493 3. If the disturbance frequency threshold was set too large, such as 4 and 5, some real forest disturbances

494 were also deleted, as shown in zoomed area B (the black oval of the last column of Fig. 8). In general,
 495 the occurrence of false positives is always ephemeral, but real forest disturbances will present
 496 continuously as bare land (or low-density vegetation) for several months (e.g., 3 months). Therefore, an
 497 appropriate frequency threshold value of 2 or 3 is suggested for the proposed method to eliminate some
 498 false positives in the adjusted monthly forest disturbance map.



499
 500 Fig. 8. An illustration of monthly forest disturbance maps with different numbers of post disturbance monthly
 501 confirmations ranging from 1 to 5 months in the spatio-temporal filter to eliminate many false positives. See text for
 502 explanation of black ovals and codes A and B.

503 5. Discussion

504 5.1 Timeliness of Planet NICFI monthly forest disturbance map

505 Timeliness is essential for the estimation of forest disturbances, particularly for near real-time
 506 monitoring systems, but there is always a trade-off between the accuracy and timeliness of forest
 507 disturbance mapping (Bullock et al., 2022; Francini et al., 2020; Tang et al., 2019; Zhu et al., 2020). As
 508 illustrated in the above results, the possible monthly forest disturbance map has the advantage of alerting
 509 to forest loss once the latest monthly Planet NICFI image is available, but the predicted forest
 510 disturbances have small confidence due to the commission error (e.g., false positives) caused by
 511 remaining clouds, registration errors and spectral outliers. The adjusted monthly forest disturbance map
 512 can increase the accuracy and confidence of estimated forest disturbances, but this decreases the

513 timeliness and increases the omission error (e.g., false negatives), and we can only adjust the forest
514 disturbances three or more months after the first occurrence. Therefore, it is suggested to use
515 simultaneously the possible and adjusted monthly forest disturbance maps in real applications. Besides
516 the delay influenced by our proposed algorithm, the observation lag and data processing lag are two
517 primary sources for determining the timeliness of forest disturbance monitoring. Although it is possible
518 to calculate the observation lag if the satellite has standard revisit times and can penetrate clouds (Bullock
519 et al., 2022), the cloud-free observation lag of Planet NICFI images can hardly be predicted due to the
520 widespread clouds in southern CAM. The spatial distribution of annual precipitation shown in Fig. 1(c)
521 is expected to match that of the observation lag for Planet NICFI images. Specifically, CAM's western
522 coastal areas, which are covered by frequent clouds and rain all year round, have the longest observation
523 lag, and the observation lag will be extended in the rainy season lasting from May to November. Once
524 the latest monthly Planet image is released in the GEE platform by NICFI, the proposed method can be
525 used to monitor monthly forest disturbances. To improve the efficiency of data processing, the entire
526 study area of CAM was divided into 214 grid cells, and it would require about one week to complete all
527 the data processing based on one GEE account. However, by dividing the 214 grid cells into several parts
528 within more GEE accounts, the data processing lag can be shortened.

529 **5.2 Limitation and uncertainty**

530 To improve the mapping of small-scale forest disturbances caused by selective logging and
531 smallholder clearing, we developed a rHue_forest index and spatio-temporal filter to monitor possible
532 and adjusted monthly forest disturbances from Planet NICFI images, but some limitations remain. Firstly,
533 although the proposed rHue_forest index is based on the Hue index (Francini et al., 2020) and aims to
534 reduce the effect of clouds and cloud shadows to some extent, it is still sensitive to the frequent clouds
535 and cloud shadows in the tropics that were not perfectly removed. Secondly, the adjusted monthly forest
536 disturbance map produced by the spatio-temporal filter can eliminate many false positives in most cases,
537 but it will also delete some real forest disturbances if clouds are extremely frequent. There is always a
538 trade-off in achieving both small commission (false positives) and omission (false negatives) errors for
539 a forest disturbance monitoring system (Bullock et al., 2022). Moreover, the cloud masks based on the
540 cloud cover possibility map and the HOT index may also incorrectly delete some real forest disturbance
541 in the monthly Planet NICFI images. These two aspects will lead to an underestimation of forest

542 disturbance in some local regions, such as the west coast areas with abundant rainfall and clouds in CAM.
543 Thirdly, the proposed rHue_forest index is sensitive to spectral change in the tree canopy cover, meaning
544 that forest disturbances may be over-estimated if there exist some deciduous forests or forests with strong
545 phenology features (e.g., flowering) in the humid forest cover map in 2020. Fourth, although the adjusted
546 monthly forest disturbance map produced by the spatio-temporal filter can eliminate many false positives
547 in the possible map, it requires three months of Planet images after the first disturbance occurrence time.
548 Fifth, if the forest degradation causes a slight tree canopy change in the Planet sub-pixel scale and there
549 is no obvious forest cover change, it may also be difficult for the proposed method to tackle. In this
550 situation, a specific method of time-series Normalized Difference Fraction Index based on spectral
551 unmixing could be used to monitor tropical forest degradation (Bullock et al., 2020; Souza et al., 2005).

552 The primary humid forest cover map in 2020 is a prerequisite for the proposed rHue_forest index
553 used to estimate the monthly forest disturbance map, and then its uncertainty will propagate to the final
554 monthly forest disturbance maps (Esteban et al., 2020). In fact, the humid tropical forest cover map in
555 2001 (Turubanova et al., 2018), annual forest loss map during 2001-2020 in GFC product (Hansen et al.,
556 2013), Sentinel-1 forest disturbances map during 2019-2020 (Reiche et al., 2021), Landsat tree canopy
557 height map in 2020 (Potapov et al., 2021) and Sentinel-2 land cover map in 2020 (Zanaga et al., 2021)
558 were fused to generate the primary humid forest cover in 2020. Each of the five typical maps has
559 uncertainty in distinguishing the primary humid forest cover, for example, the Sentinel-1 forest
560 disturbances map may be affected by the speckle noise and side-looking geometry error within Sentinel-
561 1 SAR images (Reiche et al., 2021), and their uncertainties were contained finally in the humid forest
562 cover map. Moreover, the coarser spatial resolutions and poorer spectral discrimination of the five
563 thematic maps compared to the 5 m four bands of Planet NICFI image will also lead to the uncertainty
564 in the humid forest cover map, and result in some false positives of disturbance in 2021. However, as
565 listed in Table 3, the stable humid forest in 2020 has PA and UA values of $88.71 \pm 2.72\%$ and $98.75 \pm$
566 1.09% , which means that combining the five thematic maps can predict humid forest cover in 2020 with
567 high accuracy.

568 To further decrease the uncertainty of the humid forest cover map in 2020, as shown in Fig. 2, we
569 used the Planet NICFI image in December 2020 to exclude some of the false positives of forest
570 disturbances in 2021 caused by the pixels misclassified as humid forest cover in 2020. However, the
571 areas that are masked by clouds in the Planet NICFI image of December 2020 carry no information with

572 which to exclude the false positives of disturbances related to uncertainty in the humid forest cover map.
573 To solve this problem, one could focus on increasing the accuracy (especially the user's accuracy) of the
574 humid forest cover map, to increase the accuracy of the resultant Planet NICFI monthly forest disturbance
575 map. It is, therefore, of great interest to apply some powerful methods (e.g., machine learning and deep
576 learning-based classifiers) to time-series Planet NICFI images to further decrease the uncertainty of the
577 humid forest cover map in 2020, and thereby increase the accuracy of the Planet monthly forest
578 disturbance mapping.

579 **5.3 Future research**

580 Compared with the forest disturbance maps based on RADD Sentinel-1 and GFC Landsat, the
581 developed Planet NICFI possible and adjusted monthly forest disturbance maps also cannot find the
582 forest loss that occurred in all time periods, as shown in section 4.2. However, the developed Planet
583 NICFI monthly forest disturbance maps have great potential to complement existing forest cover change
584 products, and it is, therefore, of great interest to have a combination of our product and many other forest
585 disturbance alerts in future applications, so as to provide more accurate monitoring of small-scale tropical
586 forest disturbances. Removing perfectly the clouds in Planet images with only four bands is a challenging
587 task, especially for tropical regions with extremely frequent clouds (Roy et al., 2021). Shendryk et al.
588 (2019) proposed a deep learning-based classification method to estimate clouds and cloud shadows in
589 Planet images. Wang et al. (2021) proposed an automated method to remove the clouds and cloud
590 shadows in daily 3 m PlanetScope satellite sensor images in tropical areas. These two advanced
591 approaches can be applied to the monthly Planet NICFI images to further remove the clouds and cloud
592 shadows, and future research should focus on promoting these methods via the GEE platform for large-
593 scale online computation. The proposed rHue_forest index is based on the classical index of Hue, as used
594 widely for satellite sensor images with only four bands. However, many other vegetation indices based
595 on the four bands of Planet images, such as the soil adjusted vegetation index (SAVI) (Huete, 1988) and
596 the modified soil adjusted vegetation index (MSAVI2) (Qi et al., 1994), can also be applied for the
597 proposed method. In this research, we focus on the CAM to study small-scale forest disturbances caused
598 by selective logging and smallholder clearing, but it is of interest to apply the proposed method to the
599 full range of tropical forests in the Congo Basin or, indeed, pantropical, as it can monitor many of the
600 missed forest disturbances in tropical regions (Zhang et al., 2021).

601 **6. Conclusions**

602 Based on the PlanetScope Hue index proposed by Francini et al. (2020), this research developed a
603 method, which is composed mainly of the rHue_forest index and spatio-temporal filter, to monitor
604 monthly small-scale tropical humid forest disturbances with Planet NICFI images in CAM. The proposed
605 method produced possible monthly forest disturbances in CAM with the best producer's accuracy of
606 $96.85 \pm 2.65\%$ but least user's accuracy of $21.37 \pm 16.91\%$, while the adjusted monthly forest
607 disturbances with the best user's accuracy of $84.67 \pm 2.89\%$ and a producer's accuracy of $61.46 \pm 46.43\%$.
608 Compared to the equivalent forest disturbances based on RADD Sentinel-1, GLAD Landsat and the GFC
609 product, our results were able to estimate more forest disturbances arising from selective logging and
610 smallholder clearing with greater spatial detail. Many narrow logging roads and the spatial expansion
611 process of smallholder clearing were also well represented by the proposed method. By using the
612 stratified sampling and estimators, we have produced and reported statistically rigorous estimates of
613 humid forest disturbances in CAM, estimated as $1,168 \pm 882 \text{ km}^2$ in 2021. These advantages arise
614 because Planet images have a daily revisit time, leading to the greatest possible number of images for
615 compositing the monthly Planet NICFI mosaics with a spatial resolution of 5 m. The proposed method
616 based on Planet NICFI images has great potential to complement existing forest cover change products
617 and estimate hitherto neglected small-scale tropical forest disturbances. We will share publicly the
618 possible and adjusted monthly forest disturbance map in 2021 for CAM once the paper has been
619 published.

620 **Acknowledgments**

621 The authors wish to thank the NICFI for providing the monthly Planet images and thank Francini et al.
622 (2020) for applying successfully the PlanetScope Hue index in forest change detection. This research
623 was supported by the Key Research Program of Frontier Sciences, Chinese Academy of Sciences (ZDBS-
624 LY-DQC034), National Natural Science Foundation of China (42271400, 62071457), the Hubei
625 Provincial Natural Science Foundation of China for Distinguished Young Scholars (2022CFA045), the
626 Hubei Provincial Natural Science Foundation of China (2020CFB233), the joint Postdoctoral Program
627 of China Scholarship Council and Lancaster University during 2021-2023, the Young Top-notch Talent
628 Cultivation Program of Hubei Province, and the Yellow Crane Talent Program of Wuhan.

629 **References:**

630 Asner, G.P., Knapp, D.E., Broadbent, E.N., Oliveira, P.J.C., Keller, M. and Silva, J.N., 2005. Selective
631 Logging in the Brazilian Amazon. *Science*, 310(5747): 480-482.

632 Baccini, A., Walker, W., Carvalho, L., Farina, M., Sulla-Menashe, D. and Houghton, R.A., 2017. Tropical
633 forests are a net carbon source based on aboveground measurements of gain and loss. *Science*,
634 358(6360): 230-234.

635 Betts, M.G. et al., 2017. Global forest loss disproportionately erodes biodiversity in intact landscapes.
636 *Nature*, 547(7664): 441-444.

637 Breiman, L., 2001. Random Forests. *Machine Learning*, 45(1): 5-32.

638 Bullock, E.L., Healey, S.P., Yang, Z., Houborg, R., Gorelick, N., Tang, X. and Andrianirina, C., 2022.
639 Timeliness in forest change monitoring: A new assessment framework demonstrated using
640 Sentinel-1 and a continuous change detection algorithm. *Remote Sens. Environ.*, 276: 113043.

641 Bullock, E.L., Woodcock, C.E. and Olofsson, P., 2020. Monitoring tropical forest degradation using
642 spectral unmixing and Landsat time series analysis. *Remote Sens. Environ.*, 238: 110968.

643 Cheng, Y., Vrieling, A., Fava, F., Meroni, M., Marshall, M. and Gachoki, S., 2020. Phenology of short
644 vegetation cycles in a Kenyan rangeland from PlanetScope and Sentinel-2. *Remote Sens.*
645 *Environ.*, 248: 112004.

646 Cochran, W.G., 1977. Sampling techniques. John Wiley & Sons.

647 Dong, J., Xiao, X., Sheldon, S., Biradar, C., Duong, N.D. and Hazarika, M., 2012. A comparison of forest
648 cover maps in Mainland Southeast Asia from multiple sources: PALSAR, MERIS, MODIS and
649 FRA. *Remote Sens. Environ.*, 127: 60-73.

650 Esteban, J., McRoberts, R.E., Fernández-Landa, A., Tomé, J.L. and Marchamalo, M., 2020. A Model-
651 Based Volume Estimator that Accounts for Both Land Cover Misclassification and Model
652 Prediction Uncertainty. *Remote Sens.*, 12(20): 3360.

653 Francini, S., McRoberts, R.E., Giannetti, F., Mencucci, M., Marchetti, M., Scarascia Mugnozza, G. and
654 Chirici, G., 2020. Near-real time forest change detection using PlanetScope imagery. *Eur. J.*
655 *Remote Sens.*, 53(1): 233-244.

656 Franke, J., Navratil, P., Keuck, V., Peterson, K. and Siegert, F., 2012. Monitoring Fire and Selective
657 Logging Activities in Tropical Peat Swamp Forests. *IEEE J. Sel. Top. Appl. Earth Obs. Remote*
658 *Sens.*, 5(6): 1811-1820.

659 Frazier, A.E. and Hemingway, B.L., 2021. A Technical Review of Planet Smallsat Data: Practical
660 Considerations for Processing and Using PlanetScope Imagery. *Remote Sens.*, 13(19).

661 Gibson, L. et al., 2011. Primary forests are irreplaceable for sustaining tropical biodiversity. *Nature*,
662 478(7369): 378-381.

663 Hansen, M.C., DeFries, R.S., Townshend, J.R.G., Sohlberg, R., Dimiceli, C. and Carroll, M., 2002.
664 Towards an operational MODIS continuous field of percent tree cover algorithm: examples
665 using AVHRR and MODIS data. *Remote Sens. Environ.*, 83(1): 303-319.

666 Hansen, M.C. et al., 2016. Humid tropical forest disturbance alerts using Landsat data. *Environ. Res.*
667 *Lett.*, 11(3): 034008.

668 Hansen, M.C. et al., 2013. High-Resolution Global Maps of 21st-Century Forest Cover Change. *Science*,
669 342(6160): 850-853.

670 Hethcoat, M.G., Carreiras, J.M.B., Edwards, D.P., Bryant, R.G. and Quegan, S., 2021. Detecting tropical
671 selective logging with C-band SAR data may require a time series approach. *Remote Sens.*
672 *Environ.*, 259: 112411.

673 Hethcoat, M.G., Edwards, D.P., Carreiras, J.M.B., Bryant, R.G., França, F.M. and Quegan, S., 2019. A

674 machine learning approach to map tropical selective logging. *Remote Sens. Environ.*, 221: 569-
675 582.

676 Huete, A.R., 1988. A soil-adjusted vegetation index (SAVI). *Remote Sens. Environ.*, 25(3): 295-309.

677 Kleinschroth, F., Laporte, N., Laurance, W.F., Goetz, S.J. and Ghazoul, J., 2019. Road expansion and
678 persistence in forests of the Congo Basin. *Nat. Sustainability*, 2(7): 628-634.

679 Langner, A. et al., 2018. Towards Operational Monitoring of Forest Canopy Disturbance in Evergreen
680 Rain Forests: A Test Case in Continental Southeast Asia. *Remote Sens.*, 10(4).

681 Laporte, N.T., Stabach, J.A., Grosch, R., Lin, T.S. and Goetz, S.J., 2007. Expansion of Industrial Logging
682 in Central Africa. *Science*, 316(5830): 1451-1451.

683 McRoberts, R.E., Stehman, S.V., Liknes, G.C., Næsset, E., Sannier, C. and Walters, B.F., 2018. The
684 effects of imperfect reference data on remote sensing-assisted estimators of land cover class
685 proportions. *ISPRS J. Photogramm. Remote Sens.*, 142: 292-300.

686 Olofsson, P., Foody, G.M., Herold, M., Stehman, S.V., Woodcock, C.E. and Wulder, M.A., 2014. Good
687 practices for estimating area and assessing accuracy of land change. *Remote Sens. Environ.*,
688 148: 42-57.

689 Pal, M., 2005. Random forest classifier for remote sensing classification. *Int. J. Remote Sens.*, 26(1):
690 217-222.

691 Pascual, A., Tupinambá-Simões, F., Guerra-Hernández, J. and Bravo, F., 2022. High-resolution planet
692 satellite imagery and multi-temporal surveys to predict risk of tree mortality in tropical eucalypt
693 forestry. *J. Environ. Manage.*, 310: 114804.

694 Potapov, P. et al., 2021. Mapping global forest canopy height through integration of GEDI and Landsat
695 data. *Remote Sens. Environ.*, 253: 112165.

696 Qi, J., Chehbouni, A., Huete, A.R., Kerr, Y.H. and Sorooshian, S., 1994. A modified soil adjusted
697 vegetation index. *Remote Sens. Environ.*, 48(2): 119-126.

698 Qin, Y. et al., 2019. Improved estimates of forest cover and loss in the Brazilian Amazon in 2000–2017.
699 *Nat. Sustainability*, 2(8): 764-772.

700 Reiche, J. et al., 2021. Forest disturbance alerts for the Congo Basin using Sentinel-1. *Environ. Res. Lett.*,
701 16(2): 024005.

702 Roy, D.P., Huang, H., Houborg, R. and Martins, V.S., 2021. A global analysis of the temporal availability
703 of PlanetScope high spatial resolution multi-spectral imagery. *Remote Sens. Environ.*, 264:
704 112586.

705 Sexton, J.O. et al., 2013. Global, 30-m resolution continuous fields of tree cover: Landsat-based rescaling
706 of MODIS vegetation continuous fields with lidar-based estimates of error. *Int. J. Digital Earth*,
707 6(5): 427-448.

708 Shendryk, Y., Rist, Y., Ticehurst, C. and Thorburn, P., 2019. Deep learning for multi-modal classification
709 of cloud, shadow and land cover scenes in PlanetScope and Sentinel-2 imagery. *ISPRS J.*
710 *Photogramm. Remote Sens.*, 157: 124-136.

711 Shimada, M., Itoh, T., Motooka, T., Watanabe, M., Shiraiishi, T., Thapa, R. and Lucas, R., 2014. New
712 global forest/non-forest maps from ALOS PALSAR data (2007–2010). *Remote Sens. Environ.*,
713 155: 13-31.

714 Souza, C., Firestone, L., Silva, L.M. and Roberts, D., 2003. Mapping forest degradation in the Eastern
715 Amazon from SPOT 4 through spectral mixture models. *Remote Sens. Environ.*, 87(4): 494-
716 506.

717 Souza, C.M., Roberts, D.A. and Cochrane, M.A., 2005. Combining spectral and spatial information to

718 map canopy damage from selective logging and forest fires. *Remote Sens. Environ.*, 98(2): 329-
719 343.

720 Stehman, S.V., 2014. Estimating area and map accuracy for stratified random sampling when the strata
721 are different from the map classes. *Int. J. Remote Sens.*, 35(13): 4923-4939.

722 Tang, X., Bullock, E.L., Olofsson, P., Estel, S. and Woodcock, C.E., 2019. Near real-time monitoring of
723 tropical forest disturbance: New algorithms and assessment framework. *Remote Sens. Environ.*,
724 224: 202-218.

725 Turubanova, S., Potapov, P.V., Tyukavina, A. and Hansen, M.C., 2018. Ongoing primary forest loss in
726 Brazil, Democratic Republic of the Congo, and Indonesia. *Environ. Res. Lett.*, 13(7): 074028.

727 Tyukavina, A. et al., 2018. Congo Basin forest loss dominated by increasing smallholder clearing. *Sci.*
728 *Adv.*, 4(11): eaat2993.

729 Vancutsem, C. et al., 2021. Long-term (1990–2019) monitoring of forest cover changes in the humid
730 tropics. *Sci. Adv.*, 7(10): eabe1603.

731 Wagner, F.H. et al., 2019. Using the U-net convolutional network to map forest types and disturbance in
732 the Atlantic rainforest with very high resolution images. *Remote Sens. Ecol. Conserv.*, 5(4):
733 360-375.

734 Wang, J. et al., 2021. Automatic cloud and cloud shadow detection in tropical areas for PlanetScope
735 satellite images. *Remote Sens. Environ.*, 264: 112604.

736 Watanabe, M., Koyama, C.N., Hayashi, M., Nagatani, I., Tadono, T. and Shimada, M., 2021. Refined
737 algorithm for forest early warning system with ALOS-2/PALSAR-2 ScanSAR data in tropical
738 forest regions. *Remote Sens. Environ.*, 265: 112643.

739 Zanaga, D. et al., 2021. ESA WorldCover 10 m 2020 v100. ESA WorldCover project

740 Zhang, Y., Foody, G.M., Ling, F., Li, X., Ge, Y., Du, Y. and Atkinson, P.M., 2018. Spatial-temporal
741 fraction map fusion with multi-scale remotely sensed images. *Remote Sens. Environ.*, 213: 162-
742 181.

743 Zhang, Y., Guindon, B. and Cihlar, J., 2002. An image transform to characterize and compensate for
744 spatial variations in thin cloud contamination of Landsat images. *Remote Sens. Environ.*, 82(2):
745 173-187.

746 Zhang, Y. et al., 2019. Mapping annual forest cover by fusing PALSAR/PALSAR-2 and MODIS NDVI
747 during 2007–2016. *Remote Sens. Environ.*, 224: 74-91.

748 Zhang, Y. et al., 2021. Tracking small-scale tropical forest disturbances: Fusing the Landsat and Sentinel-
749 2 data record. *Remote Sens. Environ.*, 261: 112470.

750 Zhao, F. et al., 2022. Monthly mapping of forest harvesting using dense time series Sentinel-1 SAR
751 imagery and deep learning. *Remote Sens. Environ.*, 269: 112822.

752 Zhu, Z. and Woodcock, C.E., 2014. Continuous change detection and classification of land cover using
753 all available Landsat data. *Remote Sens. Environ.*, 144: 152-171.

754 Zhu, Z., Zhang, J., Yang, Z., Aljaddani, A.H., Cohen, W.B., Qiu, S. and Zhou, C., 2020. Continuous
755 monitoring of land disturbance based on Landsat time series. *Remote Sens. Environ.*, 238:
756 111116.

757